




# An in-flight plasma diagnostic package for spacecraft with electric propulsion

Thomas Trottenberg<sup>1\*</sup> , Florian Bansemer<sup>2</sup>, Stephan Böttcher<sup>1</sup>, Davar Feili<sup>3</sup>, Hartmut Henkel<sup>2</sup>, Marcel Hesse<sup>2</sup>, Holger Kersten<sup>1</sup>, Tony Krüger<sup>1</sup>, Jens Laube<sup>4</sup>, Alexey Lazurenko<sup>5</sup>, Daniel Sailer<sup>5</sup>, Björn Schuster<sup>1</sup>, Lars Seimetz<sup>1</sup>, Alexander Spethmann<sup>1</sup>, Stefan Weis<sup>5</sup> and Robert F. Wimmer-Schweingruber<sup>1</sup>

\*Correspondence:

[trottenberg@physik.uni-kiel.de](mailto:trottenberg@physik.uni-kiel.de)

<sup>1</sup>Institute of Experimental and Applied Physics, University of Kiel, Leibnizstraße 19, D-24098 Kiel, Germany

Full list of author information is available at the end of the article

## Abstract

The plasma diagnostics presented in this article target the plasma surrounding a spacecraft that is created by the electric thruster and its surface modifying effects. The diagnostic package includes a retarding potential analyzer, a plane Langmuir probe, and an erosion sensor. The paper describes the instrument as well as suitable test environments for mimicking the effects expected in space and shows test results. The system is to fly for the first time on the Heinrich Hertz satellite, which is scheduled to be launched in 2023. The spacecraft will be equipped with a pair of Highly Efficient Multistage Plasma Thrusters (HEMPT) and a pair of Hall thrusters for redundancy.

**Keywords:** Plasma diagnostics, Electric spacecraft propulsion, Ion thrusters, Sputtering, Charge-exchange collisions

## Introduction

Electric propulsion is becoming the standard drive technology for satellites. In contrast to conventional chemical engines, the currently most frequently used “fuel” is xenon, an inert gas, which undergoes no chemical reaction and therefore does not contain any energy for the thrust generation. Instead, solar-electric power is used to ionize the propellant and electrostatically accelerate the ions. This way, much higher exhaust velocities are achieved than in case of chemical engines, where the effective exhaust velocity is roughly the thermal speed of the burned hot gas. Since the exhaust velocity also has the physical meaning of force (thrust) per mass flow rate, this important quantity is usually named the specific impulse in the field of electric propulsion. The propellant consumption for a particular mission will therefore be much less if electric engines are applied.

The most common electric thruster types are ion thrusters like Hall Effect Thrusters (HET) and Gridded Ion Thrusters (GIT), and the long-standing electrothermal thrusters like arcjets [1, 2]. HETs and GITs produce the ions by the intermediate step of a plasma from which the ions are extracted. To compensate for the permanent loss of positive

charge due to the ejected ions, a neutralizer, or cathode, is used that releases electrons into the exhaust plume.

Plasma based thrusters inherently suffer from a certain amount of neutral gas that unintentionally leaks through the open side of the discharge channel in case of HETs or through the grid holes in case of GITs. The neutral gas interacts with the accelerated ions by means of collisions, in particular by charge-exchange collisions. The latter generate ions with low thermal velocities that form a secondary plasma surrounding the spacecraft (the primary plasma meaning the neutralized exhaust plume) [3]. This secondary, thruster-generated plasma is addressed by the here described *Electric Propulsion Diagnostics Package* (EPDP) for electrically driven spacecraft.

The plasma surrounding the spacecraft attains, as all low-temperature plasmas, a positive potential with respect to the spacecraft. Therefore, the initially cold, i.e. gas temperature, ions can be accelerated and fall back onto the spacecraft. Close to the thruster exit, where the secondary ions are created, the potential is typically still several tens of volts above the spacecraft potential [4, 5], so that the ions can reach the spacecraft surface with energies above the sputter threshold.

Spacecraft often carry sensitive instruments, solar panels and other subsystems that might be disturbed or degraded by the unintended backflow from the applied thruster. The problem is not unique to electric thrusters, it was already known for chemical engines long before the time of electric propulsion systems [6]. Therefore, it is reasonable and important to ask for such undesired effects in the case of electric propulsion systems, too, and in particular when a new thruster type enters the market.

Similar attempts to evaluate energetic ion backflow and its surface modifying effects have been made before [7]. The Deep Space 1 mission, launched in 1998 and solar electrically propelled by a gridded ion thruster, already carried a diagnostic package with twelve sensors, including quartz crystal microbalances for an assessment of surface deposition or erosion, calorimeters, a retarding potential analyzer (RPA), and a planar as well as a spherical Langmuir probe (LP) for diagnostics of the plasma environment [8, 9]. The in-flight measurements proved the significance of a thruster-induced plasma environment; current densities of  $0.1 \mu\text{A cm}^{-2}$  were measured near the thruster exit during the operation of the thruster. One of the findings was that molybdenum from the thruster grids was deposited on the spacecraft surfaces. After 2750 h of thruster operation, a sensor in direct line-of-sight to the thruster collected a thin film of about 25 nm width, while a shadowed sensor still measured a 2.5 nm layer.

An in-flight diagnostic system for such effects was also part of the SMART-1 mission launched in 2003 that was driven by a xenon Hall thruster [7, 10]. That electric propulsion diagnostic package consisted of an RPA, a spherical LP, and a small solar cell and a quartz microbalance as contamination sensors. The measured ion energy distributions of the backflow exhibited a dominant population with energies about 35 eV; but there was also a plateau with approximately 15 % of the peak rate that extended to approximately 60 eV, from where it decreased and vanished at 90 eV [10]. The floating cathode (neutralizer) of the Hall thruster attained potentials ranging from  $-5 \text{ V}$  up to  $+10 \text{ V}$  along the orbit. The measured erosions were low.

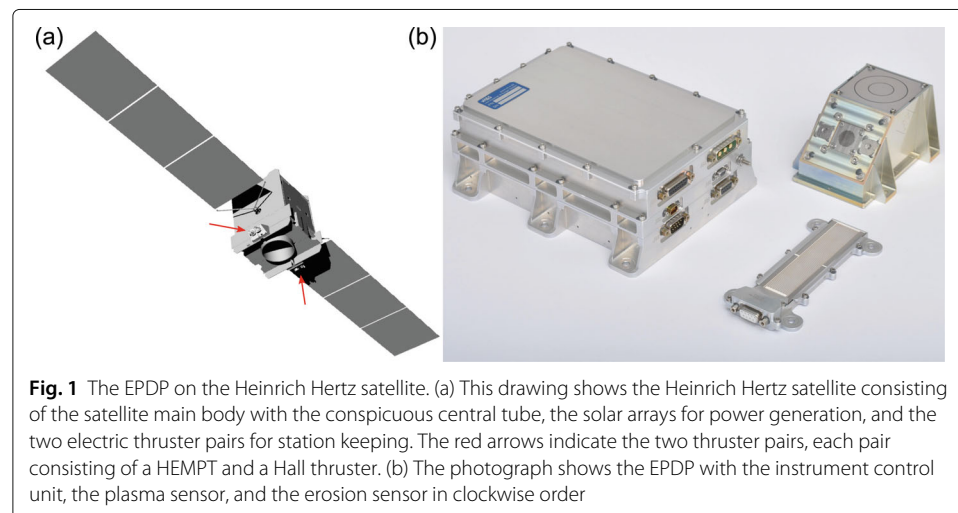
We want to emphasize the importance of in-flight measurements when it comes to the thruster-generated secondary plasma. The backflow of ions to the spacecraft is a very small unintended side effect that can hardly be imitated in test facilities. In contrast to

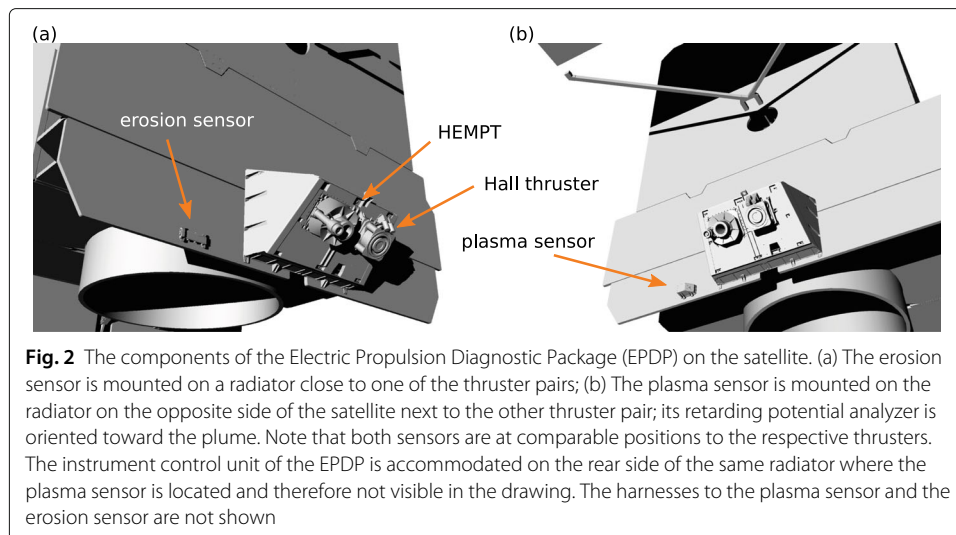
the situation in space, where the plasma is only in contact with the satellite and can expand freely, chamber walls constitute a plasma confinement due to the plasma sheaths. Moreover, the neutral gas distributions are obviously very different in space and in a test chamber, and it is precisely the gas atoms and their interaction with the accelerated ions that is the cause of the plasma surrounding the spacecraft.

In this contribution, we report on a joint collaboration of von Hoerner & Sulger GmbH, OHB System AG, and the Christian-Albrechts-Universität zu Kiel for the development of a generic Electric Propulsion Diagnostic Package for satellites propelled by a variety of electric thrusters. The system is planned to fly for the first time on the Heinrich Hertz communications satellite that is scheduled to be launched in 2023 (see Fig. 1). It will also be the first time that a Highly Efficient Multistage Plasma Thruster (HEMPT) will be employed in space [11, 12].

The Heinrich Hertz mission, financed by the German Aerospace Center (DLR) and currently being built in Bremen under the lead of OHB as system integrator, aims to explore and test new communication technologies in space at a technical and scientific level. The mission also offers universities, research institutes and industry a platform for conducting numerous scientific and technical experiments. Heinrich Hertz will be equipped with a pair of HEMPT 3050 thrusters from Thales Deutschland GmbH [13] and a pair of SPT 100 Hall thrusters from OKB Fakel [14] for redundancy (see Fig. 2).

This article has the following parts. The “[The electric propulsion diagnostic package \(EPDP\): setup and methods](#)” section provides an overview of the individual components of the diagnostics and where on the satellite they will be mounted. It follows a description of the test setup in the plasma laboratory of the Kiel University, see “[The test environment: setup and methods](#)”, and thereafter results are presented in the “[Tests of the plasma sensor: results and discussion](#)” section. The “[Tests in a HEMPT plasma: results and discussion](#)” section shows measurements in the Thales Test Facility with the EPDP plasma sensor together with the same thruster model that is intended for the Heinrich Hertz satellite. The “[Conclusion](#)” section assesses the current status of the development and summarizes the testing methods.





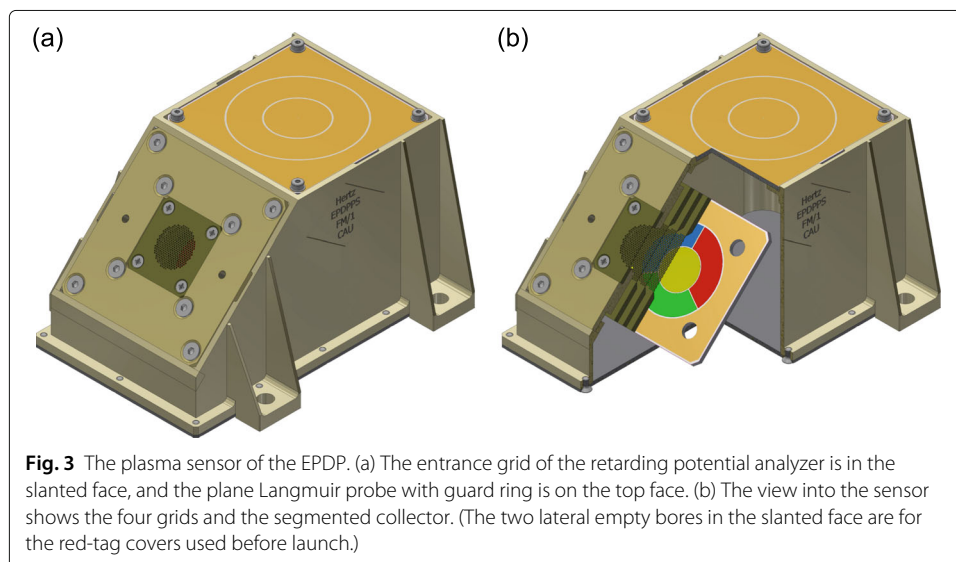
### The electric propulsion diagnostic package (EPDP): setup and methods

The EPDP consists of the plasma sensor and the erosion sensor, an instrument control unit (electronics box), two harnesses that connect the sensors to the electronics box, and a third harness that connects the box to the spacecraft.

#### The diagnostic system on the satellite

Figure 2 shows the diagnostic package (without the harnesses) and how the parts will be arranged on the Heinrich Hertz satellite.

The plasma sensor is an arrangement of an RPA and an LP in one case (see Fig. 3). The RPA will be used to measure the energy distribution function of the plasma ions that reach the satellite. It is equipped with four grids, where the outer grid is connected to spacecraft potential and integrated into the slanted surface of the common sensor head. This allows an orientation toward the thruster plume. The planar LP is integrated into the top face of



the plasma sensor. The actual probe surface is surrounded by a guard ring that is always kept by the probe electronics at the same potential as the actual probe.

The erosion sensor is based on a resistance measurement of a thin conductive layer. The change of the resistance of a silver meander is monitored during the operation of the thrusters, from which the erosion can directly be calculated. The erosion sensor has its own housing, separate from the plasma sensor [see Fig. 1(b)]. This article focuses on the plasma diagnostics part of the EPDP, i.e. the plasma sensor, so that no experimental data pertaining to the erosion sensor will be shown.

The two sensors will be located behind the thrusters, that is, where the primary plume cannot reach them (see Fig. 2). Note that plasma and erosion sensor are mounted at comparable positions relative to the respective thrusters on opposite sides of the satellite. Since the EPDP measures only at two positions on the satellite, it can consequently not provide a complete characterization of the plasma–surface interaction. To close this gap, modeling of the spacecraft environment is very important [15]. The EPDP is expected to provide reliable data for validation and improvement of numerical models.

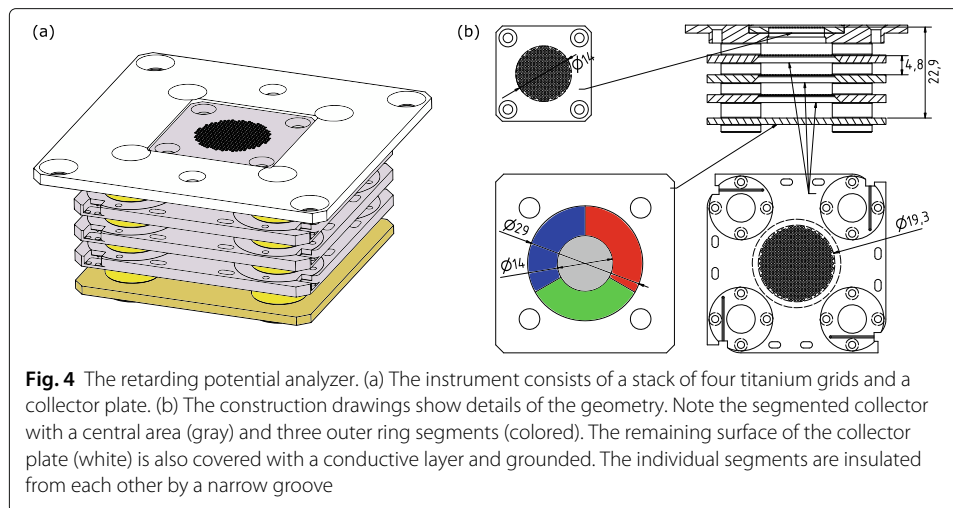
The electronics box, see Fig. 1(b), includes the main electronics of the instrument, particularly all sensor electronics, power supply, and the spacecraft interface. It contains a field-programmable gate array (FPGA), the voltage generators, measurement circuits for RPA and LP, and the resistance measurement electronics for the erosion sensor. Additionally, there are electronics measuring temperatures of two thermistors attached to LP and RPA. All voltages are generated from the DC 28 V satellite bus voltage, and the communication with the spacecraft is via an RS-422 serial interface.

The electronics box is planned to be accommodated behind one of the thruster radiators, i.e. shadowed from the thrusters. The plasma sensor is mounted on the same radiator that carries the electronics box on its back side at a distance of 55 cm from the thruster exit [see Fig. 2(b)]. The 45° slanted face of the plasma sensor, in which the RPA is integrated, points toward the center of the HEMPT exit. The erosion sensor will be attached to the other radiator diagonally opposite to the plasma sensor [see Fig. 2(a)].

### **The retarding potential analyzer**

An RPA essentially consists of a biased grid placed between the entrance and a collector plate [16, 17]. Only the charged particles with kinetic energies exceeding the grid potential overcome the potential barrier and reach the collector. The RPA can therefore be regarded as a high-pass energy filter.

In addition to the mentioned discriminating grid, more grids are necessary in order to obtain meaningful signals at the collector [18–20]. The RPA comprises four titanium grids, which can be seen in Fig. 4. The first (entrance) grid is electrically and mechanically integrated into the surface of the sensor head and therefore at spacecraft potential. The purpose of this grid is to electrostatically become part of the conductive surface of the satellite without disturbing the ambient plasma. At the same time, most of the plasma electrons are repelled in the plasma sheath between entrance grid and plasma. However, the ions accelerated by the potential drop between plasma and satellite ground will pass through the grid. Electrons with sufficient kinetic energy can overcome the potential barrier and pass through the grid, too. These electrons are to be sorted out electrostatically, otherwise their current onto the collector would partially neutralize the ion current, in which we are interested. In order to repel these electrons, the second (repeller) grid is



used; it is negatively biased, e.g. at  $-20$  V. Behind the above mentioned third (discriminator) grid, another electron repelling grid is used. This one reflects ion-induced secondary electrons that are generated at the collector surface by the ions that hit the collector. If these emitted secondary electrons were lost, their current would be misinterpreted as an additional ion current. Obviously, this grid needs to be sufficiently negative with respect to the collector, which is the potential of origin of the secondary electrons. We keep this secondary electron grid at the same negative potential as the plasma electron repeller grid by driving it with the same voltage supply.

As one can see in Fig. 4(b), the three inner grids have greater diameters (19.3 mm) than the entrance grid (14 mm). This accounts for a possible small transversal velocity component of the ions. Trajectories of obliquely entering ions could exceed the radius of the entrance grid. In the chosen design, such ions still pass through the inner grids; at the collector plane, these ions will reach one of the three outer ring segments. A simultaneous measurement of the four collector currents provides information about the direction to the place of origin of the ions.

Figure 4 also indicates the dimensions along the instrument axis: The distance from the entrance to the collector is 22.9 mm with a pairwise spacing of 4.8 mm between the inner grids and the collector.

The collector plate consists of a polyimide substrate coated with conductive layers of copper ( $50\text{ }\mu\text{m}$ ), nickel ( $5\text{ }\mu\text{m}$ ), and gold ( $0.1\text{ }\mu\text{m}$ ) from bottom up. The surface is divided into four segments by narrow, deep grooves (the remaining outer surface is grounded at spacecraft potential). The center segment collects the ions that traverse the grid system perpendicularly to the grids. In case of highly directed ions, only a small part of the current would reach the outer segments. But if there is a deviation of the incident angles from this ideal case, the three outer segments would collect different currents in an asymmetric manner.

### The plane Langmuir probe

Our design and choice for a probe type, i.e. planar, cylindrical, or spherical, result from the expected plasma densities [17, 21]. We expect densities of  $n_e = (5 \times 10^{10} \dots 1 \times$



$10^{13})\text{ m}^{-3}$ . This wide density range over more than two orders of magnitude has two major consequences for the probe design:

First, the screening lengths of the plasma have to be considered; the screening length of a plasma is known as the Debye length. In the sheath that surrounds big objects in contact with plasma or immersed in plasma, the ions are supersonically streaming onto the surface. The width of this sheath is typically several times the electron Debye length  $\lambda_{De} = (k_B T_e / n_e e^2)^{1/2}$ , which results from the electron density  $n_e$  and the electron temperature  $T_e$ . The constants  $e$  and  $k_B$  are the elementary charge and the Boltzmann constant. For the expected plasma densities, the shielding length becomes  $\lambda_{De} = 4\text{ mm} \dots 6\text{ cm}$ , assuming an electron temperature of  $k_B T_e = 3\text{ eV}$ .

Cylindrical or spherical designs require a mounting at a distance from other objects of the spacecraft longer than the shielding length. Otherwise, the probe would measure in a space charge region with complicated geometry that makes the evaluation of the collected data very difficult. A mounting of a spherical or cylindrical probe on a sufficiently long rod would also make the diagnostic mechanically much more challenging and heavier.

Fortunately, in case of a plane probe that is quasi-integrated into the spacecraft surface (actually into the EPDP sensor head), the required probe theory is much simpler. With the same objective, the actual probe surface is surrounded by a ring-shaped surface in the same plane that is kept at the same potential as the active probe surface (guard ring) by the probe electronics. This reduces the boundary effects by shifting the effective edge to larger radii. Therefore, the probe comes closer to the ideal case of a cutout of an infinite plane without boundary.

Second, the expected currents have to be considered. For example, a cylindrical probe consisting of a wire would only have a tiny surface area  $A$ , and the currents could become extremely small. On the other hand, the foreseen planar probe has an effective surface of  $A = 3.1\text{ cm}^2$ , the currents for the expected plasma densities (see above) are in the range  $I_e = 0.4\text{ }\mu\text{A} \dots 90\text{ }\mu\text{A}$  and  $I_i = 2\text{ nA} \dots 0.5\text{ }\mu\text{A}$ , which sets the requirements for the electronics.

These are two strong reasons in favor of the planar design of the LP. This kind of planar probe with guard ring is often called Faraday probe in the context of electric propulsion [22]. However, in those cases it is used as an instrument for the determination of ion beam current densities, but here, we use it as a plasma diagnostic tool, and the notion of a plane Langmuir probe therefore describes its function much better [21]. A plane Langmuir probe was also used in the Deep Space 1 mission [9].

The probe is basically a printed circuit board: It consists of a rigid polyimide laminate carrier with conductive segments for the circular active probe surface (diameter 20 mm) and an additional surrounding potential ring, or guard ring, with an outer diameter of 42 mm, as can be seen in Fig. 3; a small but deep gap insulates the two segments from each other. The conductive structures are manufactured in the same way as the RPA collector surfaces. The plate is directly mounted into the sensor head chassis.

### The erosion sensor

The purpose of the erosion sensor is to measure the erosion rate of surface material in the presence of a plasma environment. The key physical effect to be measured is the sputtering of metallic silver from an exposed detector surface due to the bombardment with particles emitted by the HEMPT.

The measurement principle of the erosion sensor is based on a resistance measurement of a thin silver layer. By measuring its resistance change over time, the erosion rate can be calculated. The silver layer in its current design is a  $2\text{ }\mu\text{m}$  thick, 1 mm wide, and 180 cm long meander, extending over an area of  $2\text{ cm} \times 10\text{ cm}$  on a rectangular ceramic substrate plate, which results in a resistance of approximately  $15\text{ }\Omega$ . The meander structure becomes necessary to increase the sensor resistance to a reasonable value compared to the wire resistance of the harness.

A photo of the erosion sensor can be seen in Fig. 1(b). The rectangular surface is the ceramic plate with the conductive thin film path. To lower thermal stress and prevent cracks of the ceramic, it is fixed by metallic springs. The erosion sensor is connected through a D-Sub connector and mounted to the spacecraft by M4 screws.

For the resistance measurement, four wires are used to remove the influence of the connecting wires by separating the stimulus wires from the sensing wires. Since the expected temperatures can range from approximately  $-80\text{ }^{\circ}\text{C}$  to  $+110\text{ }^{\circ}\text{C}$ , thermal effects are subtracted from the signal by using information from a thermistor attached to the ceramic. Possible radio-frequency disturbance from the thruster and other electromagnetic interference sources are filtered out from the measurement signal by the measurement electronics. Also a possible strong DC current flow produced by the HEMPT and solar wind effects have to be considered, which may generate a DC offset in the measurement signal; therefore, an AC measurement principle is employed. The erosion sensor has a measurement resolution of 10 nm.

We emphasize that the erosion sensor is not suitable for measuring deposition of material. Unlike a quartz microbalance, the measuring method described here can only detect erosion. If deposition is to be expected, for example of conductive grid material in the case of GITs, then the erosion sensor would not be the method of choice. A dielectric coating would hinder the measurement process, while a conductive coating would cause short circuits of the meander.

Tests, in particular for the wide range of operating temperatures, are still to be carried out and will be subject of a future publication.

### The test environment: setup and methods

In contrast to typical measurements in test chambers, the three diagnostics onboard the satellite will not be exposed directly to the thruster plume as it was explained in the section “[The Electric Propulsion Diagnostic Package \(EPDP\)](#)” (see Fig. 1). Instead, the sensors measure the *dilute backflow* from the thruster plume that feeds the plasma around the spacecraft. In order to create a plasma environment similar to the situation aboard a satellite, we use a broad-beam ion source that has been described in detail in various publications, e.g. [23, 24], and place the plasma sensor at a position *outside the beam* so that the beam will not strike the diagnostics. The sketch of the chamber in Fig. 5(a) shows the plasma sensor in such a position, denoted as “Pos. 1”.

The beam creates a population of slow ions via charge-exchange collisions with neutral gas. This population expands radially, roughly following the electric field, and fills the entire cylindrical vacuum vessel [3]. The measurements are performed in Xe at a pressure of  $(2.3 \pm 0.2) \times 10^{-2}\text{ Pa}$ , where the ion source is operated with a Xe gas flow of 7 sccm. The high-energy primary and the low-energy charge-exchange ions together with electrons predominantly stemming from a hot filament cathode form a quasi-neutral plasma [24].



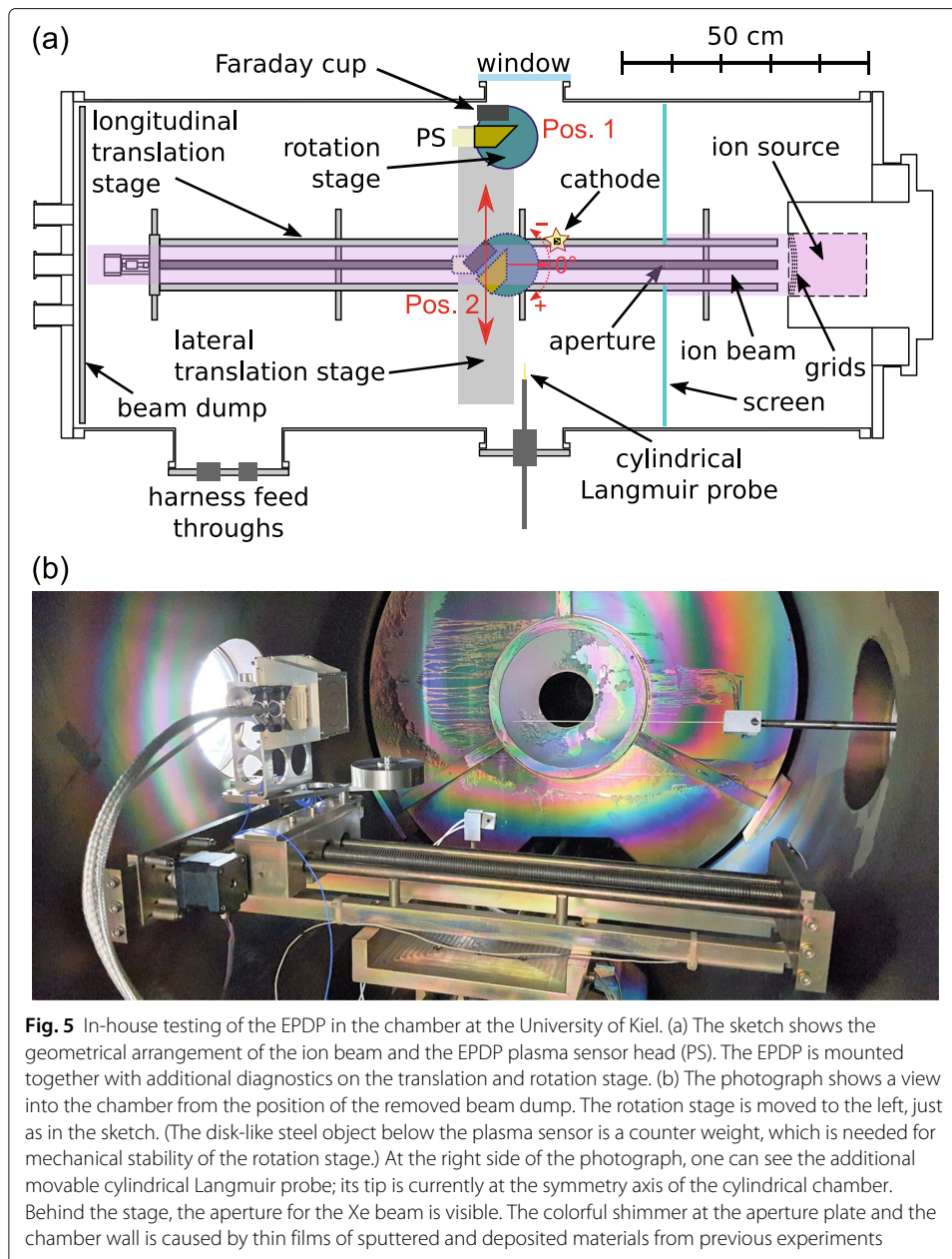


**Fig. 5** In-house testing of the EPDP in the chamber at the University of Kiel. (a) The sketch shows the geometrical arrangement of the ion beam and the EPDP plasma sensor head (PS). The EPDP is mounted together with additional diagnostics on the translation and rotation stage. (b) The photograph shows a view into the chamber from the position of the removed beam dump. The rotation stage is moved to the left, just as in the sketch. (The disk-like steel object below the plasma sensor is a counter weight, which is needed for mechanical stability of the rotation stage.) At the right side of the photograph, one can see the additional movable cylindrical Langmuir probe; its tip is currently at the symmetry axis of the cylindrical chamber. Behind the stage, the aperture for the Xe beam is visible. The colorful shimmer at the aperture plate and the chamber wall is caused by thin films of sputtered and deposited materials from previous experiments

The grid system of the broad-beam ion source [23], which extracts and accelerates the ions, consists of three spherically curved graphite grids with a curvature radius of 300 mm and a diameter of 125 mm. An antenna emits approximately 360 W of 2.4 GHz microwaves into the source chamber. The potential in the ceramic source chamber is raised by an inner ring anode and defines the accelerating potential and strong electric field in the grid system. For the tests, only two anode potentials are used: +1 200 V and 0 V.

The latter setting applies to the tests where the RPA is directly exposed to a beam of ions with lower energies; this position is denoted by “Pos. 2” in Fig. 5(a). Such a beam will be called “idling beam” in the following because no extraction voltage is applied. However, the potential in the source chamber is known to be in the order of magnitude of 100 eV

because of the plasma potential in the ion source [25], and we will confirm this by the measurements.

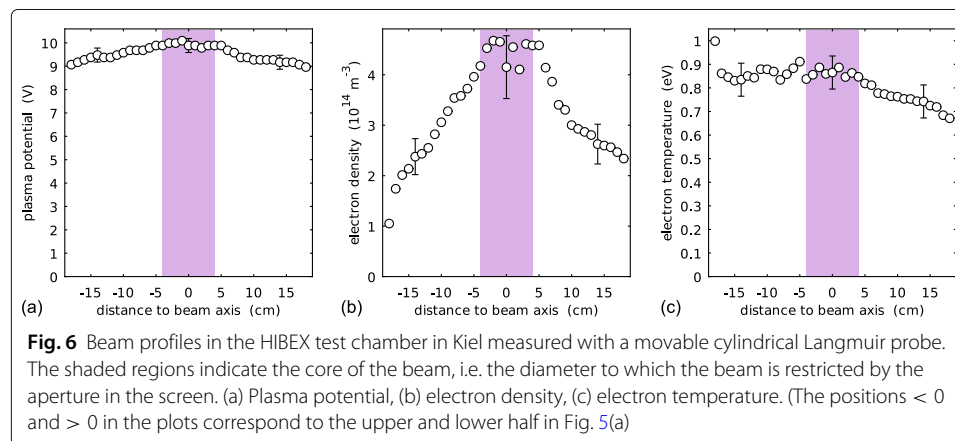
In both cases, the ion beam leaves the source at one end of the vacuum chamber, passes through the aperture in a screen, traverses the chamber and ends after a length of approximately 140 cm at the opposed beam dump. The screen with aperture reduces the beam diameter from 125 mm to 80 mm. The beam dump is made of carbon fiber velvet, which not only has a very low sputtering yield, but also a very low ion-induced (or induced by fast neutrals) secondary electron emission yield [26, 27].

The plasma sensor is mounted on the turnable and laterally movable platform together with a Faraday cup, which does not belong to the EPDP. This Faraday cup can be moved into the beam in order to measure the absolute ion flux density in the beam [see “Pos. 2” in Fig. 5(a)]; a knowledge of the absolute ion flux density is necessary for the RPA current calibration (see “Calibration of the RPA”). The distance of the RPA entrance grid and the Faraday cup aperture (diameter 5.7 mm) to the screen is 37 cm throughout the tests. An additional cylindrical Langmuir probe is mounted on a slidable feed-through. The 11 mm long probe tip made of a 100  $\mu\text{m}$  tungsten wire can be moved across the ion beam at a distance of 35 cm from the screen for a measurement of the plasma potential profile, and in particular it is used for a characterization of the plasma in front of the EPDP sensor head.

The RPA can be moved into the beam and rotated about its vertical axis until it faces the beam source, with the center of the entrance grid lying on the rotation axis. Small rotations allow the quasi-parallel ion beam to enter through the grids at variable angles. This configuration will be used for a characterization of the directivity (angular sensitivity) of the sensor (see “Directivity of the RPA”).

However, to mimic the situation on the satellite, the RPA is laterally moved to “Pos. 1” in Fig. 5(a), 18 cm away from the beam axis and rotated until its axis roughly points toward the 8-cm aperture in the screen, which imitates the thruster exit.

Figure 6 shows the profiles of the plasma potential, electron density, and electron temperature measured with the laboratory’s cylindrical Langmuir probe. Most notable is the flat potential profile, which results from the conductivity of the secondary plasma. The electron density has its maximum at the beam axis, where the beam density and



generation of charge-exchange ions has its maximum. The measurements of the electron temperature show a flat profile within the range from 0.7 eV to 0.9 eV.

### Tests of the plasma sensor: results and discussion

In this section, the measurements in the two sensor positions denoted in Fig. 5(a), i.e. beside the energetic ion beam and in the idling ion beam, are presented.

#### Outside the beam

In these experiments, RPA and LP measure outside the beam, i.e. in the position marked as “Pos. 1” in Fig. 5(a).

#### Plasma potential and ion energies

For the following measurements, the potential of the secondary plasma, from where the charge-exchange ions stem, is modified in a controlled way. The shift of the plasma potential is achieved by variations of the bias voltage of the cathode. In the test environment, the cathode is a 2.5 cm long 100- $\mu\text{m}$  tungsten wire heated by a current of 1.7 A. The positive pole of the current supply is connected to a voltage supply, which allows biasing from  $-35\text{ V}$  to  $+35\text{ V}$ . The heated wire is placed 14 cm below the beam axis and 3.5 cm shifted laterally (toward “Pos. 1”) at a distance of 23 cm from the screen (see Fig. 5).

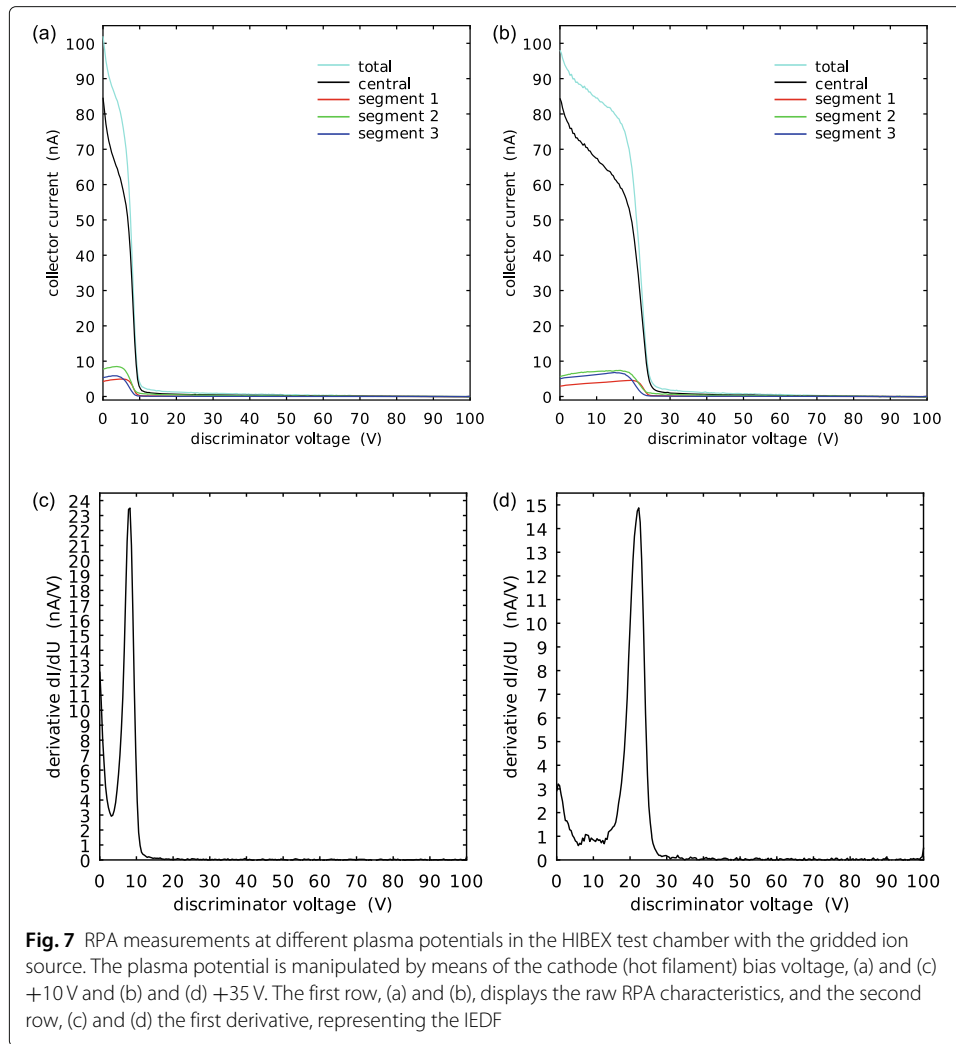
First, some exemplary RPA data is shown before the combined use of both diagnostics will be presented. Figure 7 represents two measurements with the RPA for the bias voltages  $+10\text{ V}$  and  $+35\text{ V}$ .

In the current plots, Fig. 7 (a) and (b), one can clearly distinguish two regimes: First, the regime of higher collector currents for screen grid potentials some volts below a certain threshold, and, second, the regime of almost vanishing currents for potentials some volts above that respective threshold. The first derivatives, shown in Fig. 7 (c) and (d), can be interpreted as the ion energy distribution function (IEDF): The retarding potential in volts corresponds to the energy of the singly charged ions in eV. The most abundant energy is where the derivative peaks are. (Note that the first derivatives with the unit nA/V are a measure of the rate at which ions of a given energy interval impinge on a surface, i.e. ions per  $\text{m}^2$ , s, and eV, which is different from the number density per energy interval in a volume element, i.e. ions per  $\text{m}^3$  and eV.)

One can clearly notice the shift of the curves on the discriminator voltage axis. The IEDFs exhibit narrow peaks, which indicates that the ions that reach the RPA are approximately monoenergetic. The energy of the ions shifts from 8.0 eV to 22.5 eV. We will gain a somewhat deeper understanding of the effect of the cathode bias when we come to the combined use of RPA, LP, and the additional cylindrical Langmuir probe.

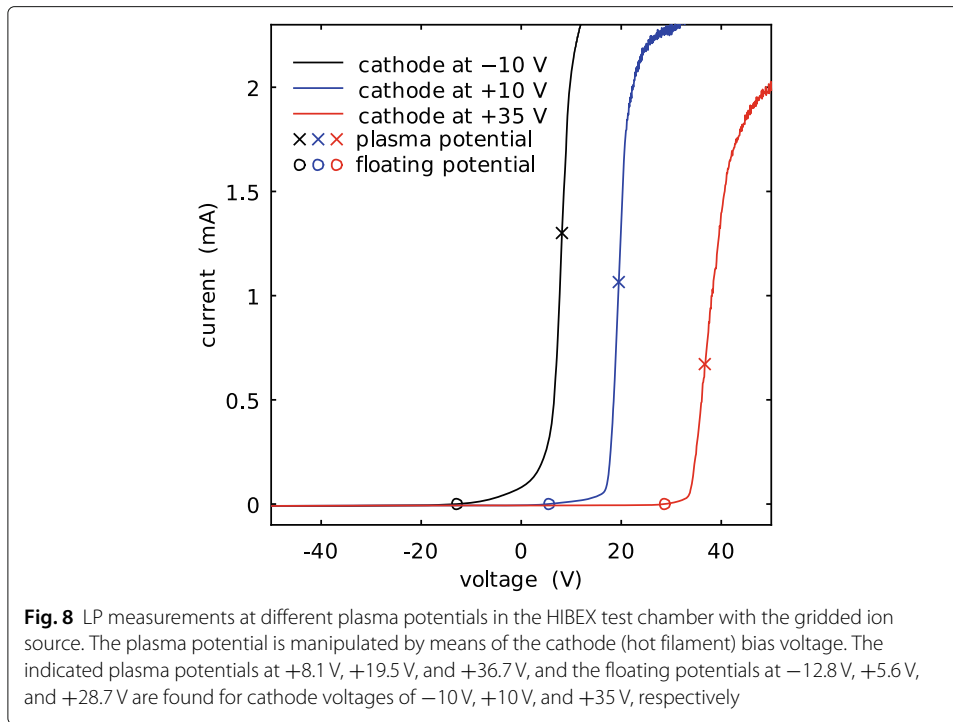
First, however, we look at the raw characteristics obtained by the LP. The three characteristics in Fig. 8 result from cathode potentials of  $-10\text{ V}$ ,  $+10\text{ V}$  and  $+35\text{ V}$ . For each curve, the “x” markers indicate the inflection point, which is taken as at the plasma potential, and the “o” symbols mark the roots of the curves, i.e. the floating potentials. Note that the characteristics are shifted toward positive voltages for increasing cathode potentials, where the shift is notably less than the increase of the hot cathode potential. We will look into this correlation in more detail.

Figure 9(a) shows the plasma potential measurements with the two Langmuir probes. The cylindrical probe was placed at the other side of the beam at the same distance to



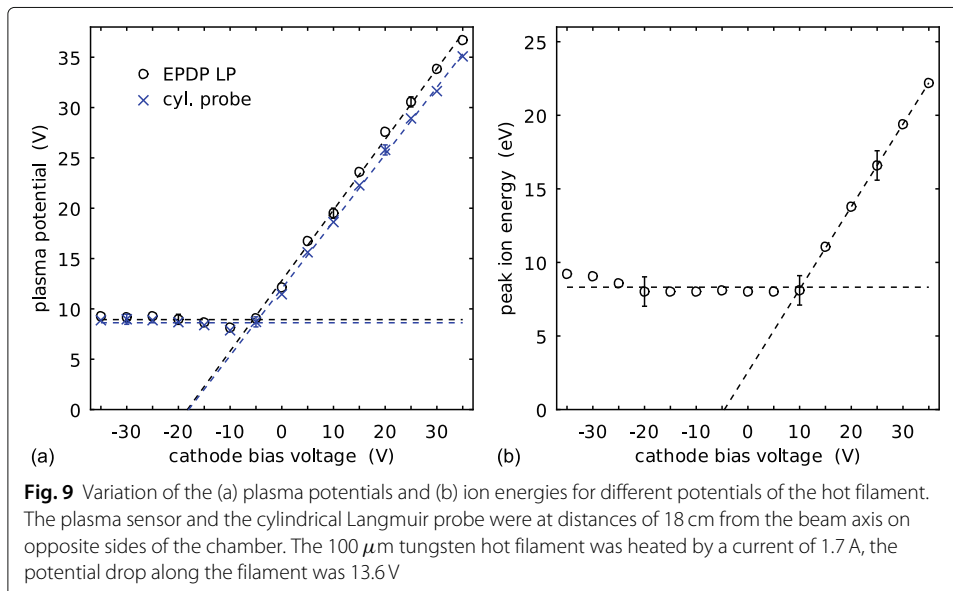
the beam axis as the plasma sensor, i.e. 18 cm. Because of the symmetry of the chamber, we expect similar plasma conditions at the positions of both Langmuir probes, which is confirmed by the two data sets: Both probes measure nearly the same plasma potentials.

More interesting is the dependence of the plasma potential on the cathode bias voltage: For  $< 0$  V at the cathode, the plasma potential remains stable at  $(8.8 \pm 0.4)$  V. This means that the injected electrons, which fall from the negative hot filament potential into the attractive plasma, do not affect much its potential. The emitted electrons traverse the plasma and are absorbed by the walls: The hot filament and the walls act like a thermionic diode. In this case, plasma and filament can maintain different potentials. The situation changes for cathode potentials  $\geq 0$  V, at which the electrons are trapped in the chamber, because the electric field in the plasma sheaths reflects them. Now, the hot filament is “connected” to the plasma via the plasma electrons (not the thermionic electrons): The filament in the plasma resembles a second diode, whose forward direction is for positive filament voltages with respect to the plasma potential. In this regime, the plasma potential increases linearly with the cathode bias voltage with a slope of approximately 0.7 for both probes. Finally, the plasma sheath at the chamber walls acts as a diode, too: For shifted plasma potentials  $U$  below the undisturbed plasma potential, the electron current across



the sheath increases exponentially with the potential shift (the current is proportional to the Boltzmann factor  $\exp(eU/k_B T_e)$ ). This effectively prevents plasma potentials from being shifted below approximately +8 V.

Figure 9(b) displays the ion energies obtained from the quasi-simultaneous RPA measurements. Here, the behavior is similar: The energy profile is roughly flat at  $(8.3 \pm 0.5)$  eV for the negative cathode bias voltages and linearly increasing with increasing positive cathode bias voltages (0.56 eV per V). However, the transition between the two regimes



seems to be shifted by approximately 10 V in the positive direction. This could find an explanation in the different plasma potentials at the hot filament position and at the beam positions where the ions are created by charge-exchange collisions.

We learned from these preliminary experiments that the application of positively biased hot filaments is a simple and efficient method to shift the plasma potential in the beam and to rise the energies of the secondary ions. On a spacecraft, such potential shifts may occur unintentionally for various reasons [10].

#### **Variation of the repeller grid voltages**

These measurements aim at a correct or optimal choice of the RPA repeller voltages. The two repeller grids are driven by the same voltage supply and connected to each other in the sensor housing; a common wire in the harness connects them to the electronics box. Figure 10 shows IEDFs for the 1.2 keV Xe ion beam with the plasma sensor still in the position “Pos. 1” in Fig. 5(a). The following can be observed:

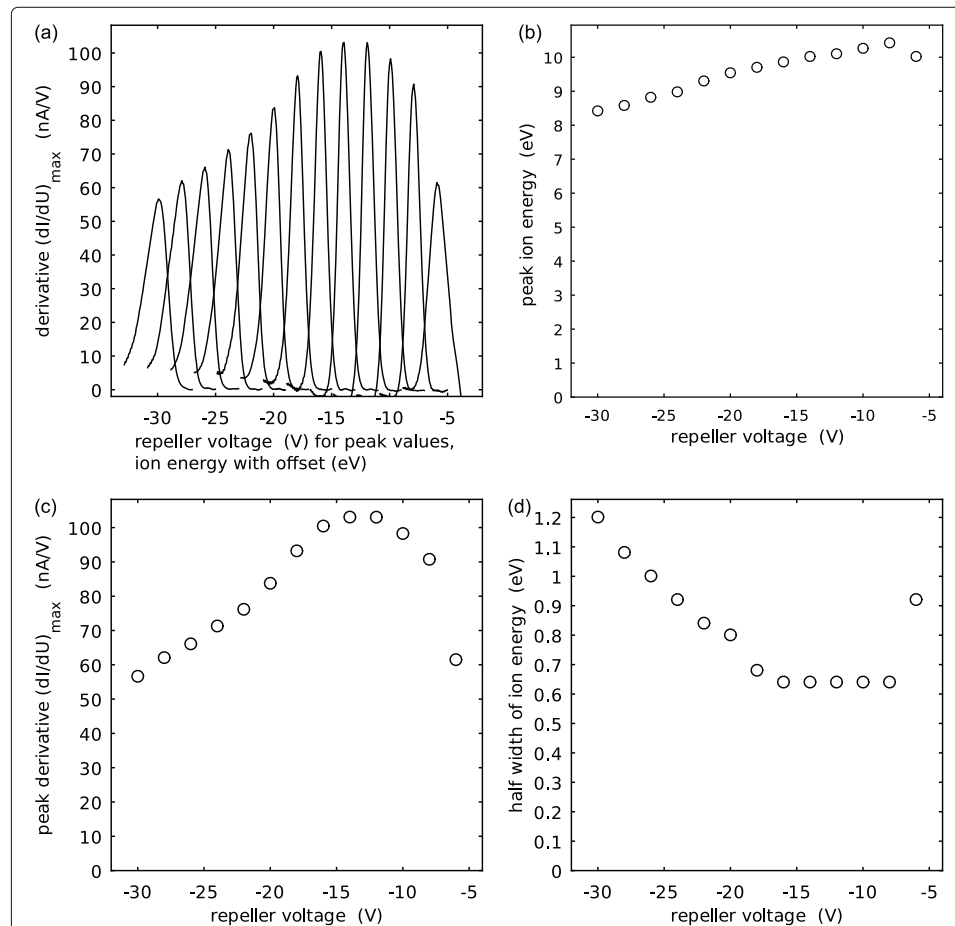


**Fig. 10** Variation of the RPA repeller grid voltage from -30 V to -5 V in steps of 1 V. These measurements were performed in the HIBEX test chamber equipped with the gridded ion source. The a hot filament cathode had a potential of -35 V. (a) Synopsis of all IEDFs. The IEDFs are horizontally shifted so that their peak values indicate the respective repeller voltage on the abscissa. (b) The peak of the measured IEDFs slightly depends on the chosen repeller voltage. (c) The height of the peak values of the IEDF reaches highest values for repeller voltages  $(-14 \pm 2)$  V. (d) The distribution functions appear sharpest for repeller voltages  $> 20$  eV



First, the determined peak ion energy (most abundant ion energy) only weakly depends on the repeller voltage; the peak energies remain within  $\pm 1$  V about the energy determined with our default repeller voltage of  $-20$  V. This is the most important result because the main purpose of the RPA is to determine the energy of the ions that return to the satellite.

Second, the peak heights and widths reach their maximum and minimum values, respectively, at a repeller voltage of only  $-15$  V. The peak width saturates at its lowest half width ( $0.6$  eV) for the repeller voltages from approximately  $-16$  V to  $-8$  V. The finding, that already moderate repeller voltages are sufficient for preventing the plasma electrons from passing through the outer repeller grid, reflects the fact that the electron temperatures are small under the given beam conditions, namely below  $1$  eV in Fig. 6(c). However, the capability of the hardware to change the repeller voltages can be used for an in-flight fine tuning of the RPA.

One has to keep in mind that the ion beam is not monoenergetic, so that the minimum measured widths of less than  $\pm 1$  eV can be used as a conservative estimate of the resolution.

#### **In the idling beam**

In the following, the RPA is moved into the beam, where it is exposed to the primary ions from the ion source. However, as described in “[The test environment: setup and methods](#)”, the anode voltage of the ion source is  $0$  V, so that only the plasma potential in the source relative to ground potential accelerates the ions.

#### **Two ion populations**

The RPA is facing directly the ion source, but is laterally moved out of the central position “Pos. 2” marked in Fig. 5(a). The panel in Fig. 11 shows collector currents and resulting IEDFs for three different positions: on the beam axis, at the edge of the beam, i.e.  $40$  mm away from the axis, and  $100$  mm away from the axis. The current profiles exhibit three discriminator grid voltage regimes separated from each other by two negative flanks, one at a low energy below  $10$  eV and another one above  $100$  eV. The flanks result in IEDFs with two peaks. The two peaks mean two ion populations, one at  $(6.5 \pm 2.0)$  eV and one at  $(107 \pm 5)$  eV, which can clearly be distinguished since they have small widths compared to their distance. This double-humped ion energy distribution function can easily be understood: The population with higher energies are the primary ions from the “idling” ion source, and the population with lower energies are the secondary, charge-exchange generated ions.

Note that the primary ions are most abundant in the center, Fig. 11 (a) and (d), reduced to less than half of that value at the edge, (b) and (e), and only marginally represented outside the beam, (c) and (f). This reflects the beam profile, to which we come back in connection with the absolute calibration of the RPA. In contrast, the secondary ions approximately stay at the same rate; this seems to be a rather complicated result of the respective “drainage volume”, the volume from where the RPA collects these ions.

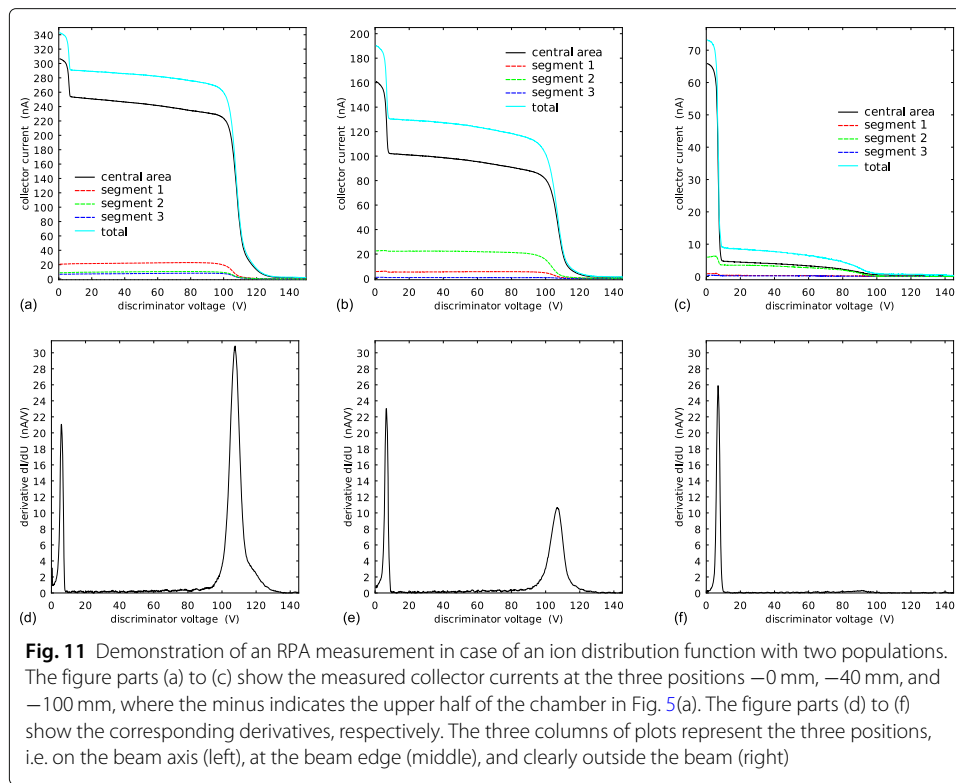


**Fig. 11** Demonstration of an RPA measurement in case of an ion distribution function with two populations. The figure parts (a) to (c) show the measured collector currents at the three positions  $-0$  mm,  $-40$  mm, and  $-100$  mm, where the minus indicates the upper half of the chamber in Fig. 5(a). The figure parts (d) to (f) show the corresponding derivatives, respectively. The three columns of plots represent the three positions, i.e. on the beam axis (left), at the beam edge (middle), and clearly outside the beam (right)

### Directivity of the RPA

The following test assesses the directivity, or angle dependent sensitivity, of the RPA. The RPA is placed in the central position “Pos. 2” marked in Fig. 5(a), i.e. at the beam axis, where it is rotated up to approximately  $25^\circ$  in both directions.

Figure 12 shows the currents measured by the collector segments at the different angles of incidence for the low energy ion beam. Two major results can be extracted from the data. First, the sensitivity of the RPA decreases within  $15^\circ$  to less than one half. (The effect of the cosine of the angle is less than 4%.) Second, the outer collector segments are very sensitive to the angle of incidence. For example, the segment 3, which is oriented in the direction in that the spot on the collector plate is shifted, reaches its maximum current value at an impact angle of approximately  $-15^\circ$ . The other two segments point  $60^\circ$  upward and downward due to the trisection of the outer segments. Therefore, segments 1 and 2 reach their respective maxima already at smaller angles of incidence than  $+15^\circ$ . The up–down asymmetry between the segments 1 and 2 seems to be due to the broken symmetry of the setup in the vertical direction. For example, the translation stages and the cathode are in the lower half of the cylindrical chamber, while the upper half is essentially empty.

### Calibration of the RPA

This test aims at a calibration of the RPA currents by means of an additional Faraday cup (see Fig. 5). The currents measured by the RPA are significantly smaller than the currents that arrive at the plane of the outer grid. A part of the ions and electrons ends at one of the four grids, and another small part, depending on the angle of incidence, reaches the collector plate beyond the collector segments.

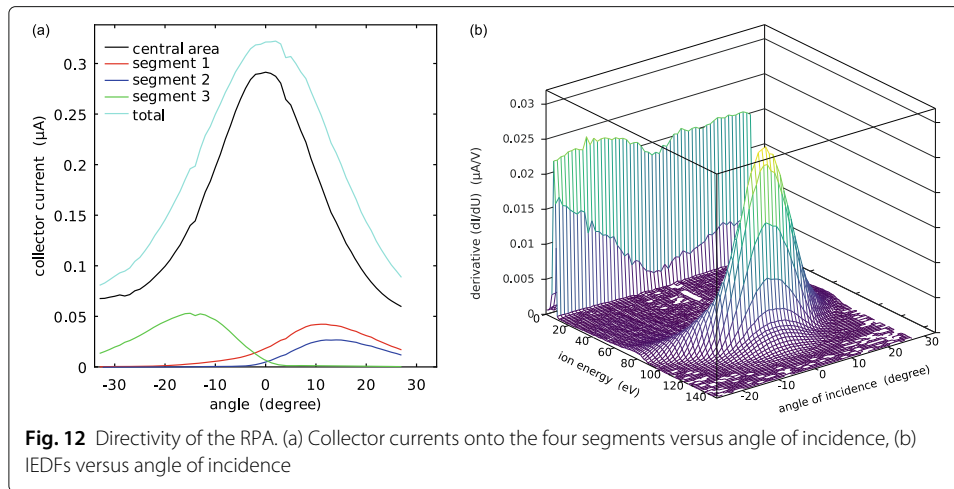


**Fig. 12** Directivity of the RPA. (a) Collector currents onto the four segments versus angle of incidence, (b) IEDFs versus angle of incidence

Moreover, the trajectories not only depend on the ion energies and directions, but also on the current density [28]. Especially the ion population with energies corresponding to the discriminator grid potential slows down to very low speeds in the vicinity of the discriminator grid. Hence, the ion density increases there significantly, which can result in a high space charge and a local potential above the discriminator grid potential. At low ion current densities, as a result of lower plasma densities, the latter effect can be neglected. In conclusion, the measured currents and the derived absolute heights of the obtained IEDF are to be interpreted with caution. (Note that this warning does not refer to the measured ion energies, but to the absolute values.)

Nevertheless, the here described method provides a conversion factor that allows a rough estimate of the ion current density from the actually measured collector currents at vanishing discriminator potentials.

Figure 13(a) shows the total current at a discriminator grid voltage of 0 V as a black curve. In this case, all ions can, at least in principle, reach one of the collector segments. The red curve depicts the total current at a discriminator grid voltage of +40 V. In this case, only ions with kinetic energies that exceed 40 eV can pass through the discriminator grid. The difference between both, i.e. the ions with kinetic energies less than 40 eV, is plotted as the blue curve.

The ions with low energy (below 40 eV) exhibit only minor variations along the path at which the RPA was moved. This reflects the presence of charge-exchange ions at all these positions. In contrast, the ions with high energy (above 40 eV) are concentrated about the beam axis and vanish completely at a distance of 100 mm from the axis. Remember that the aperture of the screen has a radius of 40 mm. The width of the Gaussian best-fit curve for the total current is approximately 40 mm, too. The energetic ions can therefore be identified as the primary ions from the ion source.

The second part of the calibration method consists of Faraday cup measurements at the same positions where the RPA measured under the same conditions. To this end, the translation stage with the two diagnostics is moved twice through the beam, the first time with the RPA directed toward the beam, and a second time, on the way back, after a rotation by  $45^\circ$ , with the Faraday cup directed toward the beam.

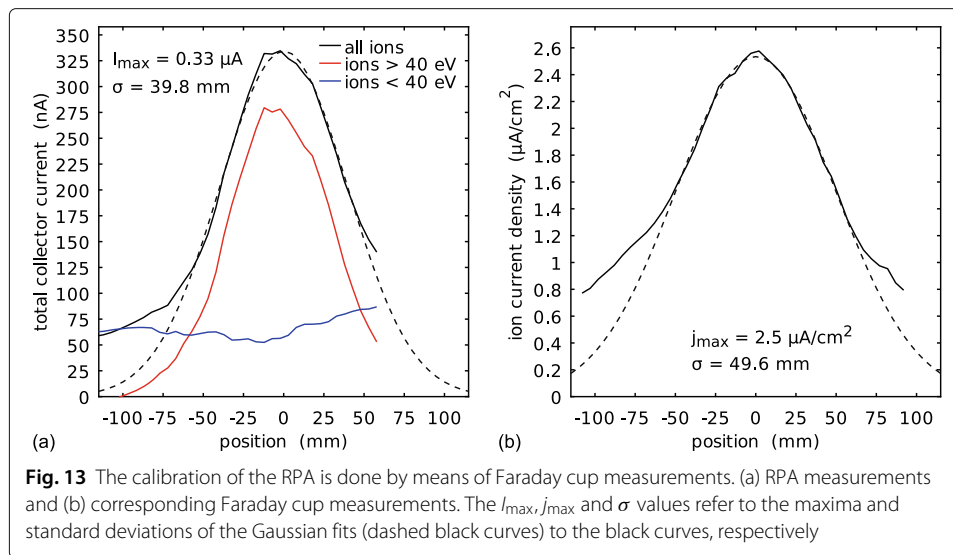


Figure 13(b) shows the resulting current densities. In case of the Faraday cup, we simply calculate the current density from the measured current and the cross section of its aperture. The profile resembles the total current measured by the RPA in that it has an inner Gaussian part for the radii up to 50 mm and a broader outer part. From the discussion of the RPA measurement, we conclude that the inner part is dominated by the energetic ions from the ion source and the outer part consists only of charge-exchange ions created in the plume.

The Gaussian best-fit curve for the Faraday cup data results in a width of approximately 50 mm. This is one quarter broader than in case of the RPA. The reason could be found in the much greater acceptance angle of the Faraday cup. At radii somewhat larger than 40 mm, which is the core radius of the beam cylinder, there are still beam ions due to the beam divergence, which we assume for an ion energy of 1.2 keV in the order of magnitude of a few degrees, probably less than  $10^\circ$  [24, 29]. These oblique energetic beam ions fully contribute to the current measured by the Faraday cup, but they are significantly attenuated by the ion optics in the RPA.

Therefore, such a calibration of the RPA currents makes only sense for perpendicularly incident ions and vanishing discriminator voltages. Taking the peak values of  $0.33 \mu\text{A}$  for the RPA and  $2.5 \mu\text{A cm}^{-2}$  for the Faraday cup at the beam axis, we obtain a calibration constant of  $7.6 \text{ cm}^{-2}$ . Multiplying the RPA currents for a discriminator voltage of 0 V and assuming merely perpendicular incidence yields a rough estimate of the current density.

We repeated this measurement with Ar instead of Xe and found the same calibration constant of  $7.6 \text{ cm}^{-2}$ .

### Tests in a HEMPT plasma: results and discussion

In this section, we report on tests of the EPDP conducted at the facility of Thales Deutschland GmbH in Ulm with a HEMPT of the type that will be installed on the Heinrich Hertz satellite. The tests are not intended to perfectly imitate the situation on the satellite in space, which is impossible. For example, even for the same relative geometrical arrangement of thruster and plasma sensor, we expect the measured plasma density in space to

be significantly lower than in the test environment. The reasons are the lower background gas density and the missing plasma confinement by potential drops at chamber walls.

The cylindrical test chamber has a diameter of 2.4 m and a length of 4.5 m and is equipped with cryogenic pumps [30]. The thruster was operated with the same settings as they will be on the satellite. For this test, two editions of the EPDP hardware were available, so that both could be used in parallel: the engineering model, which was also used in the previously described tests in the HIBEX chamber, and its predecessor, the demonstrator model. The two models differ only in that the engineering model has a mass optimized (thinner and lighter) case. The position and orientation of the engineering model sensor were chosen according to the planned installation on the satellite (see Fig. 14). The length of the line of sight from the engineering model to the plume was 36 cm. The demonstrator model sensor was placed at a different position with a distance of 55 cm to the plume.

Figure 15 shows the IEDFs measured by both RPAs. Note, that both sensors measured a double-humped IEDE, however, the population with the lower energy is much less pronounced at the position of the engineering model. One population has energies centered around 85 eV with a half width of approximately 25 eV; the other one seems to cover the entire range below 60 eV with its maximum at approximately 30 eV.

According to the setup shown in Fig. 14, there is geometrically no chance for primary plume ions to reach the RPAs. Accordingly, the ion energies are smaller than 150 eV. Therefore, one has to search for charge-exchange ions stemming from volumes where the plasma potentials are corresponding to the measured energies, i.e. potentials centered about approximately 30 V and 85 V. Simulations of HEMPTs show that the potential decreases from the thruster exit toward the neutralizer [4, 5, 31]. At the same time, this is the region of the densest plasma outside the thruster. Hence, the IEDF seems to correlate with the spatial potential distribution in the plume plasma.

Figure 16 shows the corresponding LP characteristics obtained from the two versions of the sensor. The plasma potentials are at 6.2 V and 7.2 V, respectively. The electron temperatures, obtained from the semilogarithmic plot, are 2.3 eV and 2.2 eV, respectively. The electron densities, derived from the electron temperatures and the electron saturation currents, are  $8.2 \times 10^{13} \text{ m}^{-3}$  and  $5.9 \times 10^{13} \text{ m}^{-3}$ , respectively.

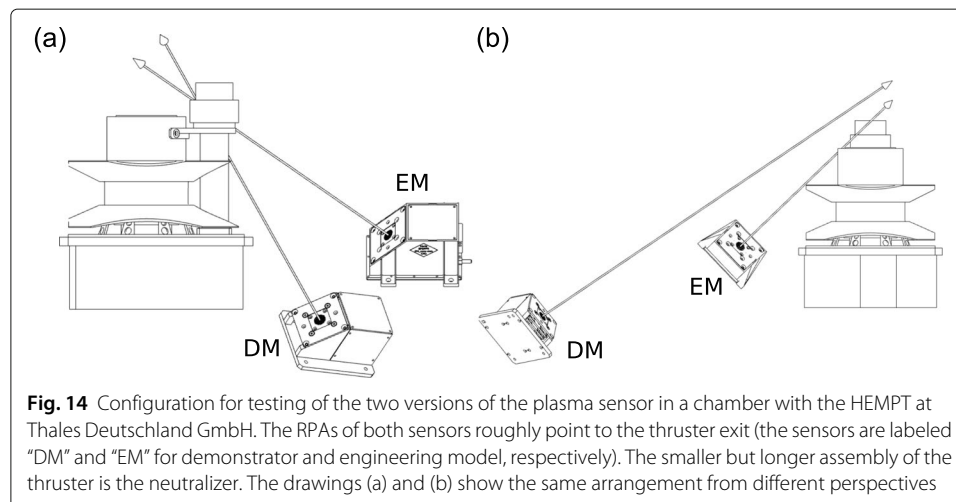
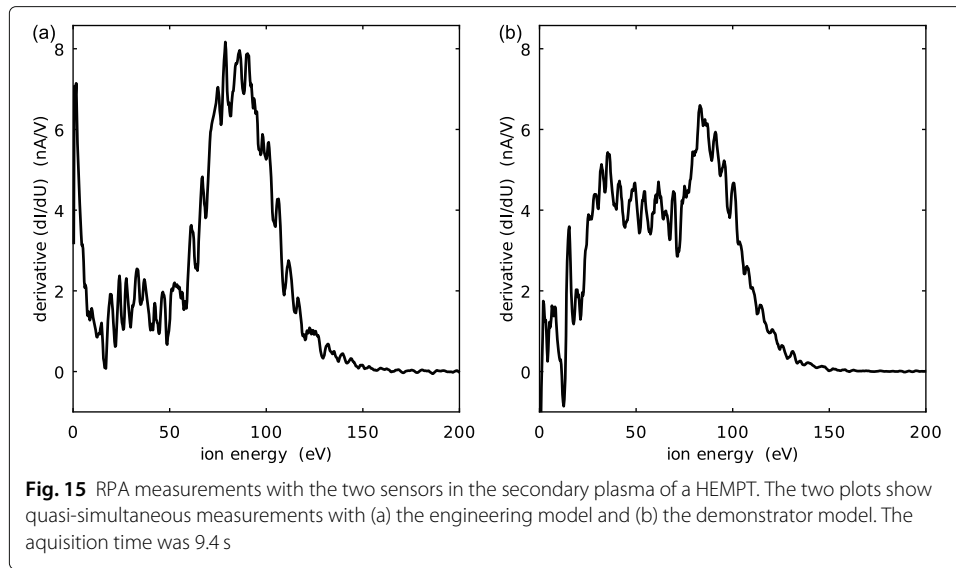
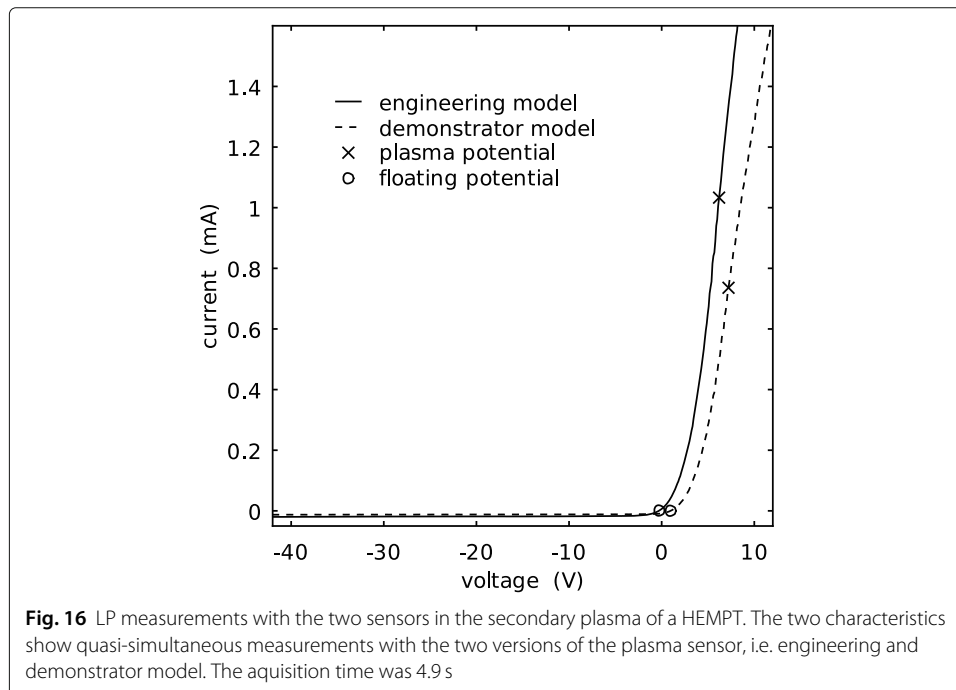


**Fig. 14** Configuration for testing of the two versions of the plasma sensor in a chamber with the HEMPT at Thales Deutschland GmbH. The RPAs of both sensors roughly point to the thruster exit (the sensors are labeled “DM” and “EM” for demonstrator and engineering model, respectively). The smaller but longer assembly of the thruster is the neutralizer. The drawings (a) and (b) show the same arrangement from different perspectives



Of special interest are the ion saturation currents, which are  $(18.5 \pm 0.5) \mu\text{A}$  and  $(12.0 \pm 0.5) \mu\text{A}$  for engineering and demonstrator model, respectively. We can attempt to determine the ion flux density from these currents using the area of the LP probe surface, which is  $3.1 \text{ cm}^2$ , and obtain  $(5.9 \pm 0.2) \mu\text{A cm}^{-2}$  and  $(3.8 \pm 0.2) \mu\text{A cm}^{-2}$ .

We can compare these flux densities with the flux densities we obtained from the calibration of the RPA (see “[Calibration of the RPA](#)”). The total collector currents for a discriminator voltage of 0 V was  $(0.42 \pm 0.01) \mu\text{A}$  coincidentally for both sensors. Application of the calibration constant of  $7.6 \text{ cm}^{-2}$  yields  $(3.2 \pm 0.1) \mu\text{A cm}^{-2}$ . The ion current fluxes measured by the RPAs are somewhat smaller than the fluxes derived from the





LP ion saturation current, but they confirm each other in the order of magnitude. The discrepancy should not surprise since the RPAs and LPs on the sensors have different orientations. Moreover, the RPA has a much smaller acceptance angle in comparison to the LP (see “[Directivity of the RPA](#)”), which becomes important for oblique incidence.

## Conclusion

A plasma diagnostic package for the particle backflow from electric thrusters to the spacecraft was presented. The three diagnostics, a retarding potential analyzer, a plane Langmuir probe, and an erosion sensor were described in detail. Tests of the two former instruments were included in this article, while the tests of the erosion sensor are still to be carried out.

A novel, suitable test environment for simulating the situation in space in an idealized form was introduced that is based on a broad-beam ion source. The neutral gas density in the beam chamber enables charge-exchange collisions between beam ions and neutral atoms. The created thermal ions flow radially out of the beam toward the cylindrical chamber wall [3]. These charge-exchange ions created along the beam are used to mimic the backflow of ions created behind the thruster to the spacecraft.

In the first part of the demonstrated testing, the plasma diagnostics were placed near the chamber wall in order to be exposed only to the secondary, charge-exchange ions, and not to the direct irradiation of the energetic beam ions.

A further feature of the test environment is the capability of controlled manipulations of the plasma potential in the beam and, related to the former, the energy of the secondary ions. This was achieved by a variable bias of the hot filament in the beam chamber, which was placed a few centimeters from the beam. It was shown that the hot filament is able to pull the plasma potential up, but it is not possible to push the plasma potential down. The behavior could be explained with the diode-like electron conductivity between filament and wall (thermionic electrons), filament and plasma (plasma electrons), and plasma and wall (sheath). Thus, the application of hot filament biases that are positive with respect to the undisturbed plasma potential is an excellent way of controlling the plasma potential in the beam. The technique was successfully applied for shifting the energies of the ions. Accordingly, the LP registered shifts of the plasma potential.

Furthermore, this satellite-like sensor position outside the beam was used for tuning the secondary electron repeller voltages of the RPA. It was found that the repeller voltages can be optimized with regard to the energy resolution, however, the determination of the peak energy of an almost monoenergetic beam was little affected by the choice of the repeller voltages.

The ion beam setup enabled another important model situation. For this purpose, the broad-beam ion source was operated without the application of an external acceleration voltage, so that a relatively weak beam with energies in the order of magnitude of only 100 eV, instead of 1.2 keV, was created. Under these conditions, it was possible to move the RPA into this “idling beam” without it being damaged. The RPA detected two ion populations with narrow energy distributions, which could be identified as the primary and secondary ions. It was confirmed by the RPA on a translation stage that the primary ions were concentrated within the beam cross-section, whereas the secondary, charge-exchange ions exhibited a flat profile across the chamber diameter.

The idling beam configuration was used, firstly, for a calibration of the RPA with the aid of an additional Faraday cup that was moved along with the RPA on the same path. A calibration constant, by which the unretarded RPA collector current can be translated into the current density measured by the Faraday cup, was successfully determined.

The idling beam was, secondly, also used for an assessment of the directivity of the RPA. The instrument was mounted on a rotation stage that enabled variable ion incidence angles. It was found that the RPA has an acceptance angle (apex) of approximately 30° (full width of half maximum), and that the segmented collector with three outer 120° ring segments is very sensitive to oblique irradiation.

The tests make the developers of the Electric Propulsion Diagnostic Package confident that its instruments will soon collect valuable data on the side effects of the thruster-generated secondary plasma. The instrument will hopefully fly on the Heinrich Hertz satellite from 2023 on.

#### Abbreviations

DLR: German Aerospace Center; ESA: European Space Agency; EPDP: Electric Propulsion Diagnostics Package; ESTEC: European Space Research & Technology Centre; FPGA: Field-Programmable Gate Array; GIT: Gridded Ion Thruster; HEMPT: Highly Efficient Multistage Plasma Thruster; HET: Hall Effect Thruster; IEDF: Ion Energy Distribution Function; LP: Langmuir Probe; RPA: Retarding Potential Analyzer

#### Acknowledgements

Not applicable.

#### Authors' contributions

FB and MH performed the development of the instrument control unit including the measurement electronics and the Erosion Sensor, supported the tests in the HIBEX chamber, and performed the test with the HEMPT. SB designed test electronics, HH is project manager and reviewed the work within the activity, DF monitored the development and testing of the EPDP, HK provided oversight and test equipment, JL performed plasma plume simulations of the HEMPT thruster, created the EPDP specification, and reviewed the EPDP development and tests during the project, AL and DS operated the test facility with the HEMPT, BS provided the electrical design, LS provided the mechanical design, AS and TK performed tests, TT wrote the paper, performed tests and data analysis, SW coordinated the tests with the HEMPT, RWS provided management, oversight, and proof reading. All authors contributed to the instrument and test design and read and approved the manuscript.

#### Funding

This work was financially supported by the European Space Agency (ESA) under GSTP Contract No. 4000126205/19/NL/RA. The instrument control unit and erosion sensor flight models will be funded by ESA, Project No. [not assigned yet], and the plasma sensor will be funded by the German Aerospace Center (DLR), Project No. 50 RS 2003. The mission specific applications of the EPDP were investigated under funding of the EPIC project within the Horizon 2020 framework program of the European Union. Open Access funding enabled and organized by Projekt DEAL.

#### Availability of data and materials

Not applicable.

#### Declarations

##### Competing interests

The authors declare that they have no competing interests.

##### Author details

<sup>1</sup>Institute of Experimental and Applied Physics, University of Kiel, Leibnizstraße 19, D-24098 Kiel, Germany. <sup>2</sup>von Hoerner & Sulger GmbH, Schlossplatz 8, D-68723 Schwetzingen, Germany. <sup>3</sup>European Space Research & Technology Centre (ESTEC), Keplerlaan 1, NL-2201 Noordwijk, Netherlands. <sup>4</sup>OHB System AG, Universitätsallee 27–29, D-28359 Bremen, Germany. <sup>5</sup>Thales Deutschland GmbH, Söflinger Straße 100, D-89077 Ulm, Germany.

Received: 9 June 2021 Accepted: 29 August 2021

Published online: 27 October 2021

#### References

1. Mazouffre S. Electric propulsion for satellites and spacecraft: established technologies and novel approaches. *Plasma Sources Sci Technol.* 2016;25:033002.
2. Wollenhaupt B, Hoa Le Q, Herdrich G. Overview of thermal arcjet thruster development. *Aircr Eng Aerosp Technol.* 2018;90:280–301.

3. Carruth Jr MR, Gabriel SB, Kitamura S. Ion Thruster Charge-Exchange Plasma Flow. *J Spacecr Rockets*. 1982;19:571–8.
4. Duras J, Kahnfeld D, Bandelow G, Kemnitz S, Luskow K, Matthias P, Koch N, Schneider R. Ion angular distribution simulation of the Highly Efficient Multistage Plasma Thruster. *J Plasma Phys*. 2017;83:595830107.
5. Kahnfeld D, Duras J, Matthias P, Kemnitz S, Arlinghaus P, Bandelow G, Matyash K, Koch N, Schneider R. Numerical modeling of high efficiency multistage plasma thrusters for space applications. *Rev Mod Plasma Phys*. 2019;3:11.
6. Chen PT, Thomson S, Woronowicz MS. Applying contamination modeling to spacecraft conventional propulsion system designs and operations. *J Spacecr Rockets*. 2001;38:388–92.
7. Capacci M, Matticari G, Noci G, Severi A, Borie D. An Electric Propulsion Diagnostic Package for the Characterization of the Plasma Thruster/Spacecraft Interactions on STENTOR Satellite. In: 35th AIAA/ASME/SAE/ASEE Joint Propulsion Conference. Los Angeles; 1999. p. AIAA–1999–2277.
8. Wang J, Brinza DE, Young DT, Nordholt JE, Polk JE, Henry MD, Goldstein R, Hanley JJ, Lawrence DJ, Shappiro M. Deep Space One Investigations of Ion Propulsion Plasma Environment. *J Spacecr Rockets*. 2000;37:545–55.
9. Brinza D, Wang J, Polk J, Henry M. Deep Space 1 Measurements of Ion Propulsion Contamination. *J Spacecr Rockets*. 2001;38:426–32.
10. González del Amo J, Estublier D, Koppel C, Capacci M, Tajmar M, Passaro A. Spacecraft/thrusters interaction analysis for Smart-1. In: 29th International Electric Propulsion Conference. Princeton; 2005. p. IEPC–2005–003.
11. Kornfeld G, Koch N, Grégory C. First test results of the HEMP thruster concept. In: 28th International Electric Propulsion Conference. Toulouse; 2003. p. IEPC–2003–212.
12. Kornfeld G, Koch N, Harmann H-P. Physics and Evolution of HEMP-Thrusters. In: 30th International Electric Propulsion Conference. Florence; 2007. p. IEPC–2007–108.
13. Koch N, Harmann H-P, Kornfeld G. Status of the THALES High Efficiency Multi Stage Plasma Thruster Development for HEMP-T 3050 and HEMP-T 30250. In: 30th International Electric Propulsion Conference. Florence; 2007. p. IEPC–2007–110.
14. Kim J-S, Kim G-H, Chung T-H, Kwon K-H. Characterization of an Oxygen Plasma by Using a Langmuir Probe in an Inductively Coupled Plasma. *J Korean Phys Soc*. 2001;38:259–63.
15. Tajmar M, González J, Hilgers A. Modeling of Spacecraft-Environment Interactions on SMART-1. *J Spacecr Rockets*. 2001;38:393–9.
16. Böhm C, Perrin J. Retarding-field analyzer for measurements of ion energy distributions and secondary electron emission coefficients in low-pressure radio frequency discharges. *Rev Sci Instrum*. 1993;64:31–44.
17. Benedikt J, Kersten H, Piel A. Foundations of measurement of electrons, ions and species fluxes toward surfaces in low-temperature plasmas. *Plasma Sources Sci Technol*. 2021;30:033001.
18. Baloniak T, Reuter R, Flötgen C, Von Keudell A. Calibration of a miniaturized retarding field analyzer for low-temperature plasmas: geometrical transparency and collisional effects. *J Phys D: Appl Phys*. 2010;43:055203.
19. Johnson SD, El-Gomati MM, Enloe L. High-resolution retarding field analyzer. *J Vac Sci Technol B*. 2003;21:350–3.
20. Simpson JA. Design of Retarding Field Energy Analyzers. *Rev Sci Instrum*. 1961;32:1283–93.
21. Mott-Smith HM, Langmuir I. The theory of collectors in gaseous discharges. *Phys Rev*. 1926;28(4):727–63.
22. Brown DL, Walker MLR, Szabo J, Huang W, Foster JE. Recommended practice for use of Faraday probes in electric propulsion testing. *J Propul Power*. 2017;33:582–613.
23. Zeuner M, Scholze F, Neumann H, Chassé T, Otto G, Roth D, Hellmich A, Ocker B. A unique ECR broad beam source for thin film processing. *Surf Coat Technol*. 2001;142:11–20.
24. Trottenberg T, Spethmann A, Rutscher J, Kersten H. Non-electrostatic diagnostics for ion beams and sputter effects. *Plasma Phys Control Fusion*. 2012;54:124005.
25. Teliban I, Trottenberg T, Schneider V, Kersten H, Neumann H, Tartz M, Scholze F. Advanced Diagnostics for Full Characterization of ECR-MW Ion Sources. In: 5th International Spacecraft Propulsion Conference. Heraklion: European Space Agency; 2008.
26. Spethmann A, Trottenberg T, Kersten H. Measurement and simulation of forces generated when a surface is sputtered. *Phys Plasmas*. 2017;24:093501.
27. Trottenberg T, Spethmann A, Kersten H. An interferometric force probe for beam diagnostics and the study of sputtering. *EPJ Techn Instrum*. 2018;5:3.
28. Talley ML, Shannon S, Chen L, Verboncoeur JP. IEDF distortion and resolution considerations for RFEA operation at high voltages. *Plasma Sources Sci Technol*. 2017;26:125001.
29. Tartz M, Hartmann E, Deltschew R, Neumann H. Effects of aperture displacement in broad-beam ion extraction systems. *Rev Sci Instrum*. 2002;73:928–30.
30. Harmann H-P, Koch N, Kornfeld G. The ULAN Test Station and its Diagnostic Package for Thruster Characterization. In: 30th International Electric Propulsion Conference. Florence; 2007. p. IEPC–2007–119.
31. Brandt T, Braxmaier C, Jansen F, Trottenberg T, Kersten H, Hey F, Johann U, Groll R. Simulation for an improvement of a down-scaled HEMP thruster. In: 34th International Electric Propulsion Conference. Kobe; 2015. p. IEPC–2015–374.

## Publisher's Note

Springer Nature remains neutral with regard to jurisdictional claims in published maps and institutional affiliations.